INEXPENSIVE SPATIAL POSITION SYSTEM FOR THE IMPROVEMENT OF MANUAL ULTRASOUND NDT

MOHAMMED ABDULLAH AL RASHED, TARIQ PERVEZ SATTAR AND OUSMANE ABDOULAYE OUMAR

Department of Engineering and Design, London South Bank University,

103 Borough Road, London SE1 0AA, UK

Manual Ultrasonic Non Destructive Testing (MUT) is vital in safety critical industries such as aerospace, chemical processing and power generation and is also well-known for its higher attainable flaw sensitivity than all other volumetric NDT (Non Destructive Testing) systems. Manual ultrasonic non-destructive testing (MUT) generally provides cost-effective and high sensitivity to flaw detection whenever short distances and/or practical access to pieces under inspection are involved. But the probability of defect detection by MUT is reduced by the influence of human factors. Therefore the aim is to improve the reliability of manual ultrasonic testing by developing an ICT enabled system based on an inexpensive spatial positioning system that during inspection will enable intelligent monitoring and performance evaluation of the human inspector, comparing the data collected from the spatial positioning system and NDT sensors against the requirements of the inspection procedure. This paper describes the development of an inexpensive wireless system comprising of an optical spatial positioning system and inertial measurement unit (IMU) that relates the 3D location of an NDT probe carried by an inspector to a computer aided drawing (CAD) representation of the test structure in a MATLAB environment and also creates images of the flaws of that test structure in three dimensions.

1. Introduction

Ultrasonic Non Destructive Testing (UT) has higher flaw sensitivity than all other volumetric NDT (Non Destructive Testing) systems. Given the essential need for robust inspection systems, and the known variability of man-machine interfaces, the reliability of manual Ultrasonic Testing (MUT) has been investigated in recent years [1,2] with a particular focus on the influence of Human Factors upon the Probability of Defect Detection (PoD). These trials have demonstrated that despite the sensitivity advantages over other technologies, the reliability of MUT is sub-optimal. Some studies have concluded that failure to correctly follow the path of inspection as stated in a qualified procedure reduces the reliability of flaw detection using MUT by 56% whilst 34% of the reduction comes from lack of acoustic coupling. The automation of NDT could increase reliability by eliminating human factors that decrease PoD. In general, studies have shown the superiority of automatic inspection over manual inspection, mainly when computerized processing techniques such as SAFT (Synthetic Aperture Focusing Technique) are added to the system [3]. Automated scanning systems include spatial measurement systems which enable the location/position and size of a detected defect to be recorded for further visits and repair. However, automated NDT scanning systems find it difficult to cope with large, complex shapes and curved surfaces whereas a human can do this more easily. The prospects of a cost effective robotic arm, which can manipulate the probe in such situations are still remote.

On the other hand, human operators are mobile and can get to difficult to access test sites to deploy a sensor probe and operate there more easily than machines. But the probe position with MUT cannot be tracked without external systems that aide a human operator to measure probe position use a range of novel positioning systems from acoustic-pulse triangulation [4] to imaging of a light mounted on a probe using a video camera [5]. The first attempt to realize a measurement system using receivers sensitive to acoustic emitters was proposed by Lund and Jensen in 1976 in [6] the well-known P-Scan system. A stable working version was created by D. Sirota in 1981 in the USSR [7] and Chang et al in 1982 in the USA [8]. Here, the receivers are placed at right angles to one another to create a coordinate reference frame. Both systems did not leave the research laboratory due in part to the impracticalities of their realization for in-service inspection. In 1996, the I-Sonic system, developed by Passi et al, [9] was able to track the position of the ultrasonic probe while also monitoring the acoustic coupling. The system has the capability to determine the swivelling of a probe to 1° resolution in the -90° to +90° range.

Optical tracking systems have also be applied in the same manner. Sensors [10] [11] (e.g. cameras) are mounted at fixed locations. Ultrasonic probes to be tracked are marked with passive or active landmarks. Such techniques are

known to be susceptible to occlusion problems, albeit, this is overcome by using additional landmarks which incidentally improve the accuracy of pose estimation. These types of position tracking systems offer highly portable solutions which scale well on any surface geometry, although many are prohibitively expensive due to the high development costs of relatively complex technologies.

MUT continues to play a big part in the NDT industry because of its ease of use and can give the required performance at a cheaper cost. No automated scanning system can match the dexterity of a human hand and arm in moving the probe over a complex shape, following a curved surface very easily and skewing the probe to get maximum signal amplitude. So, rather than developing mechanized and automated alternatives to MUT as others have, the present research aims to combine aspects of automatic systems with MUT methods.

2. Aims and Objectives

The aim is to improve the reliability of manual ultrasonic testing by developing an Information, Communication and Technology (ICT) enabled system based on a wireless spatial positioning system that during inspection will enable intelligent monitoring and performance evaluation of the human inspector, comparing the data collected from the spatial positioning system and NDT sensors against the requirements of the inspection procedure. A permanent inspection record of the plan, side and end views of a component with the flaws superimposed on the image [12,13] could then be used to create 3D images.

The objectives to meet this aim are:

- Develop very low cost systems using bulk electronic devices that capture both the precise 3D spatial position of the ultrasonic test probe relative to the test component throughout the inspection and determines its orientation by determining pitch, roll and yaw angles. The location of ultrasonic pulse echoes captured during the inspection can then be used to build 3D visualization maps.
- Develop a NDT operating system that captures both component engineering data and qualified inspection procedure data. The operating system combines CAD models of the component under test and provides instructions to the human operator when manually testing a component to carry out a specified scan pattern according to an approved procedure. It thereafter captures the actual scan pattern executed by the probe during the inspection, creating a verification of practice against specification. This system will also constitute a facility to train novice NDT operators.

3. Development of an inexpensive spatial position system

By using built-in sophisticated electronics in the Sony Wii remote controllers, a cheap but very accurate positioning system can be developed. Here we report the development of a wireless spatial positioning system that is capable of tracking the position and orientation of an ultrasonic probe relative to the component under inspection, with an accuracy of ±2mm at distances up to 5m.

Figure 1. Example test piece 1 on which ultrasonic NDT is to be performed. The spatial positioning system relates data to this object

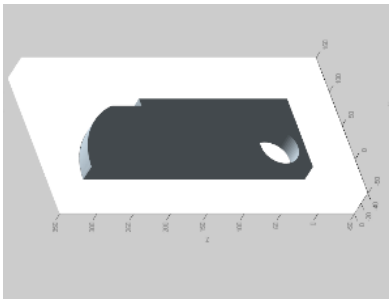

Figure 2. CAD of object imported into the MATLAB environment

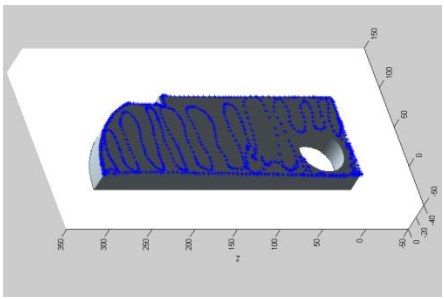

Figure 3. Probe trajectory marked on the CAD image in real time with manual deployment of probe

3.1. *Verification of concept*

To verify the concept, a small steel test piece 1 (Figure 1) was modelled and its CAD imported into the MATLAB display environment (Figure 2). The object is 300mm long and 100mm wide. First, a bench mark was created by mounting a UT probe as a tooltip to a FARO measurement arm [14] and a random motion trajectory executed by manually moving the probe. The trajectory was recorded and visualized in real-time (Figure 3) on the CAD of the test object. The system (Figure 4) now always knows where the probe tip is located relative to the test object and how the probe is oriented relative to the object surface. This information can be used to verify if a specified qualified procedure and scanning trajectory is executed by a human operator. While the FARO arm is a very precise mechanical tool to determine the orientation of the tool tip and measure spatial position x-y-z to micron accuracy, its work envelope is limited and it is very expensive. The motion of the probe is restricted by the constraints of the mechanical arm. To obtain similar capability with a physically unconstrained probe, albeit with lesser positioning accuracy, an inexpensive wireless spatial position system is required that measures probe x-y-z position and orientation. A solution is proposed in the next section that is based on recent advances in sophisticated electronic devices that are volume produced for game playing consoles and hence very cheap.

Figure 4. System comprising of the FARO arm, test object and CAD visualization

4. Wii infrared optical positioning system

Many Infrared based optical motion capture systems are commercially available in the market. e.g. iotracker [10], PhaseSpace[15], Vicon [16], ART GmbH [11], NaturalPoint [17], etc. These systems can give high precision, flexibility and high data rate. However, they cost more than tens of thousands of dollars and because of the high price those systems are not widely used. Because of the availability and cheap cost of the Wii remote (approximately 30.00 GBP), many researchers have conducted experiments using one or more Wii remotes to make a positioning system that has achieved less than +/- 2mm accuracy [18,19,20,21,22],which is enough for our proposed NDT system.

The Wii remote is a sophisticated sensor dependent controller that comprises of a MEMS 3-axis accelerometer, 3-axis gyroscope, IR camera, and Bluetooth technology for communication. The IR camera chip contains a multi object tracking engine which provides on-board processing capability to detect up to four IR LEDs with high resolution and high tracking speed. Its refresh rate is 100Hz. Experiments conducted in the lab show that the horizontal and vertical field of view of the Wii IR Camera is 45˚ and 32˚ respectively. The resolution is 128×96 pixels and the on board chip uses 8×sub pixel analysis to give the detected four IR LED blob at a resolution of 1028×768. Web cameras found in the market at the same price have lower resolution and refresh rate then the Wii infrared camera. The Wii remote returns distance coordinates and the intensity of the detected LEDs to the host PC by Bluetooth connectivity which can then be imported into the MATLAB environment by using a MEX file.

Two Wii controllers were mounted on a tripod using an aluminium extrusion bar with their field of view overlapping each other. Stereo triangulation was used to find the coordinates of a target IR LED. For stereo triangulation, the focal point of each camera must be known and for more accuracy the distortion model of each camera is required. Also required are the positions and the orientations of both cameras relative to each other. These parameters can be obtained by running a calibration process. In a two camera vision system [Figure 5], for a point P in 3D space, its $\overrightarrow{\boldsymbol{P_L}}$ and $\overrightarrow{\boldsymbol{P_R}}$ in the left and the right camera coordinates systems have the following relationship:

$$\overrightarrow{\boldsymbol{P_L}} = R_R^L \,.\, \overrightarrow{\boldsymbol{P_R}} + T_R^L \quad \text{.....Equation 1}$$

Where $\boldsymbol{R_R^L}$ is the rotation matrix and $\boldsymbol{T_R^L}$ is the translation vector that relates the left camera with the right camera of the vision system. These parameters can also be obtained by running the calibration process. To find the 3D position of points, a built-in function in the MATLAB calibration toolbox has been used. The function passes the intrinsic and extrinsic parameters along with the image projection coordinates of the points detected on the left and the right camera. The function returns a 3xN matrix of coordinates of the points in respect to the left camera reference frame and also in respect to the right camera reference frame.

For the reconstruction of 3D points from the stereo Wii camera, the linear triangulation technique [23] has been used because of its simple coding and it is the most used triangulation method. Other techniques such as the midpoint triangulation method [23] uses too many approximations therefore results are not optimal. Bundle techniques [23] on the other hand, use iterative techniques which take too much time and memory for the computation.

4.1. *Triangulation*

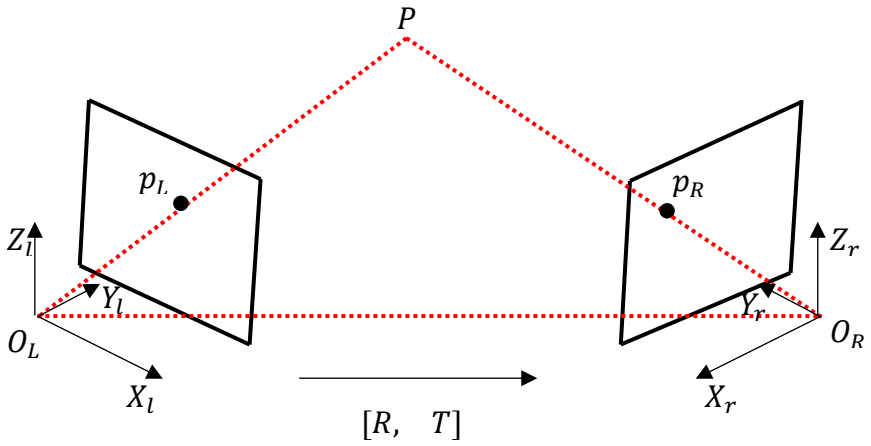

Figure 5. Geometric model of 3D point triangulation

Let $\overrightarrow{P_L} = [X_l \quad Y_l \quad Z_l]^T$ and $\overrightarrow{P_R} = [X_r \quad Y_r \quad Z_r]^T$ be the coordinate vectors of point P in the left and right camera coordinate systems respectively resulted by the perspective projection . $\overrightarrow{P_L}$ and $\overrightarrow{P_R}$ Are mapped to the left and right image coordinate systems and denoted by $\overrightarrow{p_L}$ and $\overrightarrow{p_R}$ respectively, where $\overrightarrow{p_L} = [x_l \quad y_l \quad 1]^T$, $\overrightarrow{p_R} = [x_r \quad y_r \quad 1]^T$ are the normalized homogeneous coordinates. We can relate $\overrightarrow{P_L}$ and $\overrightarrow{P_R}$ with a standard rigid motion transformation equation given by $\boldsymbol{R_R^L}$ $\boldsymbol{T_R^L}$ in Equation 1.

According to the pinhole camera model, we have

$$\overrightarrow{P_L} = Z_l.\overrightarrow{p_L} \; and \; \overrightarrow{P_R} = Z_r.\overrightarrow{p_R}.$$

Thus, Equation 1 can be rewritten as:

$$Z_l.\overrightarrow{p_L} = \boldsymbol{R_R^L}\, Z_r.\overrightarrow{p_R} + \boldsymbol{T_R^L}$$

$$-\boldsymbol{R_R^L}\, Z_r.\overrightarrow{p_R} + Z_l.\overrightarrow{p_L} = \boldsymbol{T_R^L}\text{……..Equation 2}$$

Which yields the following linear equation:

$$[-\boldsymbol{R_R^L}\overrightarrow{p_R} \quad \overrightarrow{p_L}] \begin{bmatrix} Z_r \\ Z_l \end{bmatrix} = \boldsymbol{T_R^L}\text{…….} \text{ Equation 3}$$

In this triangulation problem, 3D coordinates $\overrightarrow{P_L}$ and $\overrightarrow{P_R}$ can be obtained from the image coordinates $\overrightarrow{p_L}$ and $\overrightarrow{p_R}$ as shown in Figure 5.

Let $A = [-\boldsymbol{R_R^L}\overrightarrow{p_R} \quad \overrightarrow{p_L}]$, a 3 × 2 matrix. The least-squares solution of Equation 3 is:

$$\begin{bmatrix} Z_r \\ Z_l \end{bmatrix} = (A^T A)^{-1} A^T \boldsymbol{T_r^l}\text{…….Equation 4}$$

$$\begin{bmatrix} Z_r \\ Z_l \end{bmatrix} = \left(\begin{bmatrix} -\boldsymbol{R_R^L}\overrightarrow{p_R} \\ \overrightarrow{p_L} \end{bmatrix} [-\boldsymbol{R_R^L}\overrightarrow{p_R} \quad \overrightarrow{p_L}] \right)^{-1} \begin{bmatrix} -\boldsymbol{R_R^L}\overrightarrow{p_R} \\ \overrightarrow{p_L} \end{bmatrix} \boldsymbol{T_R^L} \text{ … … … … Equation 5}$$

From Equation 5, a closed form expression for $\begin{bmatrix} Z_r \\ Z_l \end{bmatrix}$ can be written:

$$\begin{bmatrix} Z_r \\ Z_l \end{bmatrix} = \begin{pmatrix} \left\|-\boldsymbol{R_R^L}\overrightarrow{p_R}\right\|^2 & \langle -\boldsymbol{R_R^L}\overrightarrow{p_R}, \overrightarrow{p_L}\rangle \\ \langle \overrightarrow{p_L}, -\boldsymbol{R_R^L}\overrightarrow{p_R}\rangle & \|\overrightarrow{p_L}\|^2 \end{pmatrix}^{-1} \begin{bmatrix} \langle -\boldsymbol{R_R^L}\overrightarrow{p_R}, \boldsymbol{T_R^L}\rangle \\ \langle \boldsymbol{T_R^L}, \overrightarrow{p_L}\rangle \end{bmatrix}$$

$$\begin{bmatrix} Z_r \\ Z_l \end{bmatrix} = \frac{1}{\left\|-\boldsymbol{R_R^L}\overrightarrow{p_R}\right\|^2 \|\overrightarrow{p_L}\|^2 - \langle -\boldsymbol{R_R^L}\overrightarrow{p_R}, \overrightarrow{p_L}\rangle^2} \begin{pmatrix} \|\overrightarrow{p_L}\|^2 & -\langle -\boldsymbol{R_R^L}\overrightarrow{p_R}, \overrightarrow{p_L}\rangle \\ -\langle \overrightarrow{p_L}, -\boldsymbol{R_R^L}\overrightarrow{p_R}\rangle & \left\|-\boldsymbol{R_R^L}\overrightarrow{p_R}\right\|^2 \end{pmatrix} \begin{bmatrix} \langle -\boldsymbol{R_R^L}\overrightarrow{p_R}, \boldsymbol{T_R^L}\rangle \\ \langle \boldsymbol{T_R^L}, \overrightarrow{p_L}\rangle \end{bmatrix}$$

$$\begin{bmatrix} Z_r \\ Z_l \end{bmatrix} = \begin{bmatrix} \dfrac{\|\overrightarrow{p_L}\|^2 \langle -\boldsymbol{R_R^L}\overrightarrow{p_R}, \boldsymbol{T_R^L}\rangle - \langle -\boldsymbol{R_R^L}\overrightarrow{p_R}, \overrightarrow{p_L}\rangle \langle \boldsymbol{T_R^L}, \overrightarrow{p_L}\rangle}{\left\|-\boldsymbol{R_R^L}\overrightarrow{p_R}\right\|^2 \|\overrightarrow{p_L}\|^2 - \langle -\boldsymbol{R_R^L}\overrightarrow{p_R}, \overrightarrow{p_L}\rangle^2} \\ \dfrac{-\langle \overrightarrow{p_L}, -\boldsymbol{R_R^L}\overrightarrow{p_R}\rangle \langle -\boldsymbol{R_R^L}\overrightarrow{p_R}, \boldsymbol{T_R^L}\rangle + \left\|-\boldsymbol{R_R^L}\overrightarrow{p_R}\right\|^2 \langle \boldsymbol{T_R^L}, \overrightarrow{p_L}\rangle}{\left\|-\boldsymbol{R_R^L}\overrightarrow{p_R}\right\|^2 \|\overrightarrow{p_L}\|^2 - \langle -\boldsymbol{R_R^L}\overrightarrow{p_R}, \overrightarrow{p_L}\rangle^2} \end{bmatrix}$$

$$[Z_r] = \left[\frac{\|\overrightarrow{p_L}\|^2 \langle -\boldsymbol{R_R^L}\overrightarrow{p_R}, \boldsymbol{T_R^L}\rangle - \langle -\boldsymbol{R_R^L}\overrightarrow{p_R}, \overrightarrow{p_L}\rangle \langle \boldsymbol{T_R^L}, \overrightarrow{p_L}\rangle}{\left\|-\boldsymbol{R_R^L}\overrightarrow{p_R}\right\|^2 \|\overrightarrow{p_L}\|^2 - \langle -\boldsymbol{R_R^L}\overrightarrow{p_R}, \overrightarrow{p_L}\rangle^2} \right]$$

$$[Z_l] = \left[\frac{-\langle \overrightarrow{p_L}, -\boldsymbol{R_R^L}\overrightarrow{p_R}\rangle \langle -\boldsymbol{R_R^L}\overrightarrow{p_R}, \boldsymbol{T_R^L}\rangle + \left\|-\boldsymbol{R_R^L}\overrightarrow{p_R}\right\|^2 \langle \boldsymbol{T_R^L}, \overrightarrow{p_L}\rangle}{\left\|-\boldsymbol{R_R^L}\overrightarrow{p_R}\right\|^2 \|\overrightarrow{p_L}\|^2 - \langle -\boldsymbol{R_R^L}\overrightarrow{p_R}, \overrightarrow{p_L}\rangle^2} \right]$$

Where $\langle , \rangle$ is a dot product operator. Thus

$$\widehat{P_L} = Z_l . \overrightarrow{p_L} = Z_l . \begin{bmatrix} x_l \\ y_l \\ 1 \end{bmatrix}$$

$$\widehat{P_R} = Z_r . \overrightarrow{p_R} = Z_r . \begin{bmatrix} x_r \\ y_r \\ 1 \end{bmatrix}$$

Since errors are inevitable in practice, we average the final results as follows:

$$\overrightarrow{P_L} = (\widehat{P_L} + (\boldsymbol{R_R^L} . \widehat{P_R} + \boldsymbol{T_R^L}))/\mathbf{2}$$

$$\overrightarrow{P_R} = (\widehat{P_R} + (\boldsymbol{R_R^L} . \widehat{P_L} + \boldsymbol{T_R^L}))/\mathbf{2}$$

We have used the above triangulation method to find the 3D position of the ultrasound probe. In this function, the intrinsic and the extrinsic parameters have been passed along with the image projection coordinates of the points detected on the left and the right camera. After this process is completed, the function gives a 3xN matrix of coordinates of the points in respect to the left camera reference frame and also in respect to the right camera reference frame.

5. Measurement of probe orientation

The orientation of the probe relative to the test surface is measured by an inexpensive inertial measurement unit (IMU) mounted on top of an ultrasound probe. The unit is the x-IMU that has a 3-axis accelerometer, 3-axis gyroscope and 3–axis magnetometer and Bluetooth communications built into it. The unit provides roll, pitch and yaw data. Software developed by this research creates a bridge between the x-IMU and MATLAB to obtain data to find the probe orientation in real time.

5.1. *Fusion Algorithm to get the orientation from the IMU*

The most popular algorithms available to find the orientation from an IMU or (Magnetic, Angular Rate, and Gravity) MARG sensor are Direction Cosine Matrix (DCM) algorithm [24], Kalman Filter [25] and Gradient Descent Algorithm [26]. In this research the gradient descent [26] algorithm by O.H. Madgwick has been adopted to find the orientation of the Ultrasound probe. The algorithm uses a quaternion representation, allowing accelerometer and magnetometer data to be used in an analytically derived and optimized gradient descent algorithm to compute the direction of the gyroscope measurement error as a quaternion derivative. When the sensor is static the level of accuracy is (RMS error) 0.80 and when on the move, the accuracy is (RMS error) 1.70, which is sufficient for our purposes to find the orientation of the ultrasound probe.

The orientation of the global world frame relative to the ultrasound probe frame at time t can be represented by ${}^{U}_{G}\vec{Q}_{\omega,t}$ and can be computed by numerically integrating quaternion derivative ${}^{U}_{G}\dot{Q}_{\omega,t}$ as described by Equation 6 and Equation 7, provided that the initial condition are known.

$${}^{U}_{G}\dot{Q}_{\omega,t} = \frac{1}{2} {}^{U}_{G}\vec{Q}_{est,t-1} \otimes {}^{U}\vec{\omega}_t \quad \text{.....Equation 6}$$

$${}^{U}_{G}\vec{Q}_{\omega,t} = {}^{U}_{G}\vec{Q}_{est,t-1} + {}^{U}_{G}\dot{Q}_{\omega,t}\Delta T \quad \text{.....Equation 7}$$

Here $\otimes$ is the quaternion multiplication operator, ΔT is the sampling period, $\mathrm{U}\vec{\omega}_t$ is the angular rate vector and ${}^{U}_{G}\vec{Q}_{est,t-1}$is the previous estimation of orientation. The leading subscript G denotes the global world frame and the

leading U denotes the ultrasound probe frame. The subscript ω indicate that the quaternion is calculated from the angular rates.

The quaternion ${}^{U}_{G}\vec{Q}_{\nabla,t}$ can be calculated by using the gradient decent algorithm with the accelerometer and magnetometer sensor. Further details to find ${}^{U}_{G}\vec{Q}_{\nabla,t}$ are in reference [26]. Equation 8 below calculates the estimated orientation ${}^{U}_{G}\vec{Q}_{\nabla,t}$ computed at time t based on a previous estimate of orientation ${}^{U}_{G}\vec{Q}_{est,t-1}$and the objective function error ∇f in equation 9 defined by the sensor measurements U$\vec{a}_t$ and U$\vec{m}_t$ sampled at time t.

$$ {}^{U}_{G}\vec{Q}_{\nabla,t} = {}^{U}_{G}\vec{Q}_{est,t-1} - \mu_t \frac{\nabla f}{\|\nabla f\|} \quad \text{.....Equation 8} $$

$$ \nabla f = J^{T}_{G,B}({}^{U}_{G}\vec{Q}_{est,t-1}, {}^{G}\vec{G}, {}^{G}\vec{B}) f_{G,B}({}^{U}_{G}\vec{Q}_{est,t-1}, {}^{G}\vec{G}, {}^{U}\vec{a}_t, {}^{G}\vec{B}, {}^{U}\vec{m}_t) \quad \text{.....Equation 9} $$

Equations 5, 6, 7 define the objective function f where J in Equation 9 is its Jacobian.

$$ f_{G,B}\left({}^{U}_{G}\vec{Q}_{est,t-1}, {}^{G}\vec{G}, {}^{U}\vec{a}_t, {}^{G}\vec{B}, {}^{U}\vec{m}_t\right) = \begin{bmatrix} f_{G\left({}^{U}_{G}\vec{Q}_{est,t-1}, {}^{G}\vec{G}, {}^{U}\vec{a}_t\right)} \\ f_{B\left({}^{U}_{G}\vec{Q}_{est,t-1}, {}^{G}\vec{B}, {}^{U}\vec{m}_t\right)} \end{bmatrix} \quad \text{.....Equation 10} $$

$$ f_{G\left({}^{U}_{G}\vec{Q}_{est,t-1}, {}^{G}\vec{G}, {}^{U}\vec{a}_t\right)} = {}^{U}_{G}\overrightarrow{Q^*}_{est,t-1} \otimes {}^{G}\vec{G} \otimes {}^{U}_{G}\vec{Q}_{est,t-1} - {}^{U}\vec{a}_t \quad \text{.....Equation 11} $$

$$ f_{B\left({}^{U}_{G}\vec{Q}_{est,t-1}, {}^{G}\vec{B}, {}^{U}\vec{m}_t\right)} = {}^{U}_{G}\overrightarrow{Q^*}_{est,t-1} \otimes {}^{G}\vec{B} \otimes {}^{U}_{G}\vec{Q}_{est,t-1} - {}^{U}\vec{m}_t \quad \text{.....Equation 12} $$

Here ${}^{G}\vec{G}$ and ${}^{G}\vec{B}$ are the gravitational and magnetic field vectors respectively in the global world frame. It is acceptable to compute one iteration per time sample in the condition that the convergence rate of the estimated orientation governed by step size μ_t is equal or greater than the rate of change of physical orientation.

An estimated orientation of the earth frame relative to the sensor, $\overrightarrow{{}^{U}_{G}Q_{est,t}}$ is obtained through the fusion of the two separate orientation calculations, ${}^{U}_{G}\vec{Q}_{\omega,t}$ and ${}^{U}_{G}\vec{Q}_{\nabla,t}$ as described by Equation 13 where σ_t is the weighted value.

$$ \overrightarrow{{}^{U}_{G}Q_{est,t}} = \sigma_t {}^{U}_{G}\vec{Q}_{\nabla,t} + (1-\sigma_t){}^{U}_{G}\vec{Q}_{\omega,t} \quad \text{.....Equation 13} $$

The optimal value of σ_t should ensure the weighted rate of divergence of ${}^{U}_{G}\vec{Q}_{\omega,t}$is equal to the weighted rate of convergence of ${}^{U}_{G}\vec{Q}_{\nabla,t}$. So Equation 14 can be written as

$$ (1-\sigma_t)\beta = \sigma_t \frac{\mu_t}{\Delta T} $$

$$ \sigma_t = \frac{\beta}{\frac{\mu_t}{\Delta T}+\beta} \quad \text{.....Equation 14} $$

Where $\frac{\mu_t}{\Delta T}$ is the convergence rate of ${}^{U}_{G}\vec{Q}_{\nabla,t}$ and β is the divergence rate of ${}^{U}_{G}\vec{Q}_{\omega,t}$ which is described in Equation 15.

$$ \beta = \left\| \frac{1}{2} {}^{U}_{G}\vec{Q} \otimes [0 \quad \omega_\beta \quad \omega_\beta \quad \omega_\beta] \right\| = \sqrt{\frac{3}{4}}\omega_\beta \quad \text{.....Equation 15} $$

${}^{U}_{G}\vec{Q}$ is any unit quaternion and ω_β represents the measurement error of each axis.

A large value of μ_t used in Equation 8 and 14 means ${}^{U}_{G}\vec{Q}_{est,t-1}$ and β in the denominator accordingly become negligible and then Equation 8 and 14 can be rewritten as

$$ {}^{U}_{G}\vec{Q}_{\nabla,t} \approx -\mu_t \frac{\nabla f}{\|\nabla f\|} \quad \text{.....Equation 16} $$

$$ \sigma_t \approx \frac{\beta \Delta T}{\mu_t} \quad \text{.....Equation 17} $$

Substituting Equation 7, 16 and 17 into equation 13 yields equation 18

$$ \overrightarrow{{}^{U}_{G}Q_{est,t}} = \frac{\beta \Delta T}{\mu_t}\left(-\mu_t \frac{\nabla f}{\|\nabla f\|}\right) + (1 - \frac{\beta \Delta T}{\mu_t})({}^{U}_{G}\vec{Q}_{est,t-1} + {}^{U}_{G}\dot{Q}_{\omega,t}\Delta T) $$

$$ \overrightarrow{{}^{U}_{G}Q_{est,t}} = -\beta \Delta T\left(\frac{\nabla f}{\|\nabla f\|}\right) + (1 - \frac{\beta \Delta T}{\mu_t})({}^{U}_{G}\vec{Q}_{est,t-1} + {}^{U}_{G}\dot{Q}_{\omega,t}\Delta T) \quad \text{.....Equation 18} $$

It is also possible to assume that $\frac{\Delta T}{\mu_t} \approx 0$ and Equation 18 can be simplified as Equation 19

$$ \overrightarrow{{}^{U}_{G}Q_{est,t}} \approx -\beta \Delta T\left(\frac{\nabla f}{\|\nabla f\|}\right) + ({}^{U}_{G}\vec{Q}_{est,t-1} + {}^{U}_{G}\dot{Q}_{\omega,t}\Delta T) $$

$$ \overrightarrow{{}^{U}_{G}Q_{est,t}} \approx {}^{U}_{G}\vec{Q}_{est,t-1} + \left[{}^{U}_{G}\dot{Q}_{\omega,t} - \beta\left(\frac{\nabla f}{\|\nabla f\|}\right)\right]\Delta T \quad \text{.....Equation 19} $$

It can be seen from the above equation that the algorithm calculates the orientation $\overrightarrow{{}^{U}_{G}Q_{est,t}}$ by numerically integrating the gyroscope ${}^{U}_{G}\dot{Q}_{\omega,t}$ with the magnitude of the gyroscope measurement error β, removed in a direction based on the accelerometer and magnetometer measurements. Figure 6 shows the real time captured data from accelerometer, gyroscope, magnetometer and the Euler angles obtained by passing the accelerometer, gyroscope and magnetometer data into the fusion algorithm explained above.

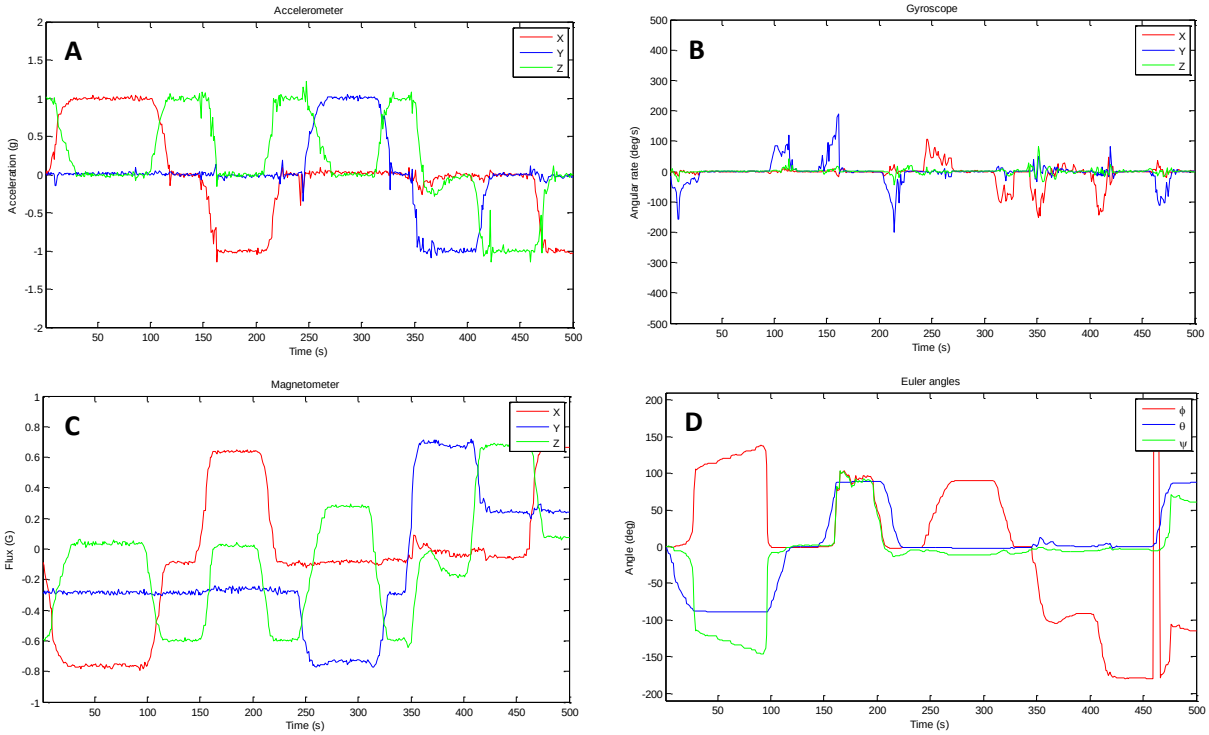

Figure 6. Real time captured data of accelerometer (image A), gyroscope (image B), Magnetometer (image C) and Euler angles (image D)

6. Wii camera calibration

Calibration of a camera means finding the intrinsic and extrinsic parameters of the camera which are needed to reconstruct the 3D structure of a scene from pixel coordinates of its image points. The parameters that define the location and orientation of the camera reference frame with respect to a known world reference frame are called extrinsic camera parameters. The parameters necessary to link the pixel coordinates of an image point with the corresponding coordinates in the camera reference frame are called intrinsic camera parameters. The intrinsic parameters characterize the optical, geometric, and digital characteristic of the camera.

For the Wii camera calibration, two open source camera calibration toolboxes have been used. The camera calibration toolbox for MATLAB [27] is capable of calibrating one or two cameras. With the multi camera self-calibration tool box [28] more than two camera calibration can be done.

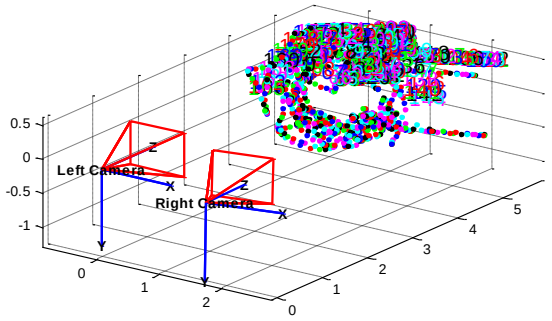

Figure 7. Calibration using square pattern of 4 IR LEDs

Calibration of stereo vision procedure

For the Wii stereo vision calibration a program was written in MATLAB to capture a calibration pattern which consists of a planar circuit board with 4 Infra Red (IR) LEDs mounted at the four corners of a 101 mm x 101mm square. Two Wii cameras capture the position of the 4 LEDs in real time with the pattern board placed in random positions and orientations. Each side of the square is assumed to be one unit. For accurate calibration more than 200 data sets of the square pattern were captured by the Wii remotes at different angles and positions (Figure 7).

7. Alignment of the probe with the IR LEDs to get the centre 3D position of the probe tip

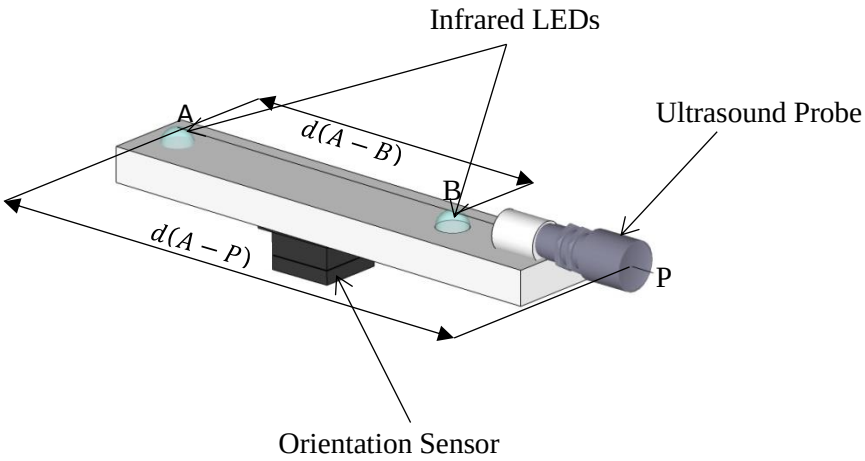

Figure 8. 3D model of the Complete System

Figure 8 shows the construction of the NDT probe spatial positioning system. It comprises of an ultrasound probe with a holder on which are mounted two IR LEDs and an IMU. The spatial positioning system will determine the coordinates of the IR LEDs. The equations to find the coordinates of the point P at the centre of the tip of the NDT probe from these coordinates are derived as follows. The centre of the ultrasound probe tip is aligned with the two IR LEDs in such a way that all of them lie on the same straight line. The parametric equations for the line can be written by knowing the coordinates (X_1, Y_1, Z_1) of the LED at location **A**, the coordinates (X_2, Y_2, Z_2) at location **B** and the probe centre P located at coordinates (X_p,Y_p Z_p), and the distances d(A-P) and d(B-P) of the LEDs at point A and point B respectively from the probe centre P.

$$\boldsymbol{X_p = X_1 + (X_2 - X_1).t} \quad \text{.....Equation 20}$$

$$\boldsymbol{Y_p = Y_1 + (Y_2 - Y_1).t} \quad \text{.....Equation 21}$$

$$\boldsymbol{Z_p = Z_1 + (Z_2 - Z_1).t} \quad \text{.....Equation 22}$$

Where t could be any real number. The distance from A to P is:

$$\boldsymbol{d(A-P) = \sqrt{\left(X_1 - X_p\right)^2 + \left(Y_1 - Y_p\right)^2 + \left(Z_1 - Z_p\right)^2}} \quad \text{.....Equation 23}$$

The coordinates of the centre of the probe tip can be unequivocally found by solving the above four equations. Now substituting the value of (X_p,Y_p Z_p) in Equation 23 yields Equation 24

$$\boldsymbol{d(A-P) = \sqrt{[X_1 - X_1 + (X_2 - X_1).t]^2 + [Y_1 - Y_1 + (Y_2 - Y_1).t]^2 + [Z_1 - Z_1 + (Z_2 - Z_1).t]^2}} \quad \text{..Equation 24}$$

$$t = \frac{\sqrt{\left(X_1 - X_p\right)^2 + \left(Y_1 - Y_p\right)^2 + \left(Z_1 - Z_p\right)^2}}{\sqrt{(X_1 - X_2)^2 + (Y_1 - Y_2)^2 + (Z_1 - Z_2)^2}}$$

$$t = \frac{d(A-P)}{d(A-B)} \quad \text{.....Equation 25}$$

Here $d(A-B)$ is the distance between two IR LEDS. Therefore the final equation for finding the centre of the probe can be written as:

$$\boldsymbol{X_p = X_1 + (X_2 - X_1).\frac{d(A-P)}{d(A-B)}} \quad \text{.....Equation 26}$$

$$\boldsymbol{Y_p = Y_1 + (Y_2 - Y_1).\frac{d(A-P)}{d(A-B)}} \quad \text{.....Equation 27}$$

$$\boldsymbol{Z_p = Z_1 + (Z_2 - Z_1).\frac{d(A-P)}{d(A-B)}} \quad \text{.....Equation 28}$$

8. Finding orientation of the probe with respect to the test piece

Orientation of the NDT probe is measured by an inertial measurement system (IMU). The IMU coordinate system in Figure 9 needs to be aligned with the test piece coordinate system to get the right orientation of the UT probe with respect to the test piece. The coordinate system of the IMU can be transferred to the test piece coordinate system by

multiplying the rotation matrix of the IMU in the world coordinate system with the rotation matrix of the IMU in the coordinate frame of the test piece. The equation below gives the orientation of the IMU with respect to the test piece.

$$O_{IMU}^{Testpiece} = \begin{bmatrix} \cos\beta\cos\gamma & \cos\gamma\sin\alpha\sin\beta - \cos\alpha\sin\gamma & \cos\alpha\cos\gamma\sin\beta + \sin\alpha\sin\gamma & 0 \\ \cos\beta\sin\gamma & \cos\beta\cos\gamma + \sin\alpha\sin\beta\sin\gamma & -\cos\gamma\sin\alpha + \cos\alpha\sin\beta\sin\gamma & 0 \\ -\sin\beta & \cos\beta\sin\alpha & \cos\alpha\cos\beta & 0 \\ 0 & 0 & 0 & 1 \end{bmatrix} \quad \text{.....Equation 29}$$

$$0_{probe}^{Testpiece} = O_{IMU}^{World} \times o_{IMU}^{Testpiece} \quad \text{.....Equation 30}$$

Where $0_{probe}^{Testpiece}$ is the orientation of the probe with respect to the test piece coordinate system, $o_{IMU}^{Testpiece}$ is the orientation of the IMU with respect to the test piece coordinate system and O_{IMU}^{World} is the orientation of the IMU with respect to the world coordinate system and α, β and γ are the roll, pitch and yaw respectively.

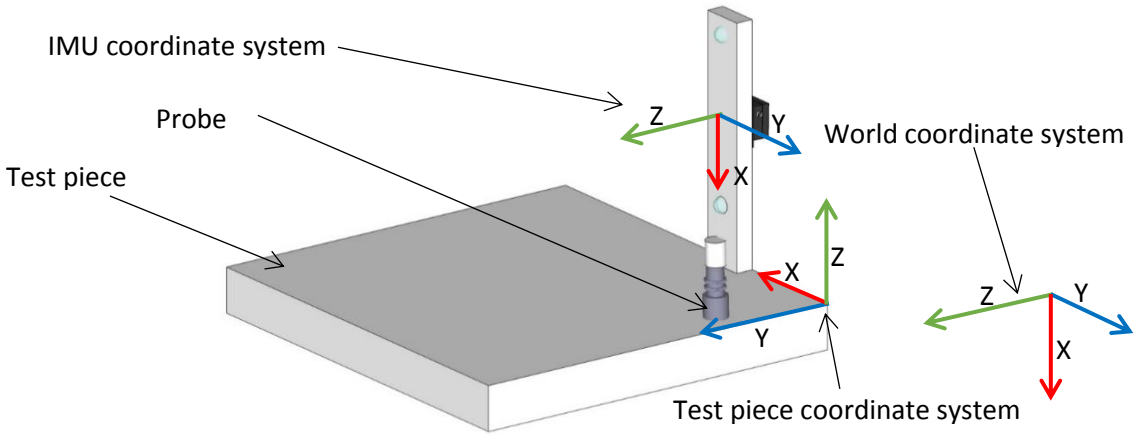

Figure 9. Finding orientation of the probe with respect to the test piece

9. Construction of a local coordinate system in 3D

For the proposed system a spatially aware device needs to be built, which is able to locate itself in space and know its orientation relative to the component under inspection. To define a coordinate system, three reference points on the Test piece surface are taken as shown in Figure 10. The full procedure to align the coordinate system from the camera to the component under inspection is given below:

Figure 10. Construction of the Local coordinate system in 3D

The reference points AA and the TS are the first two points taken on the test piece to define the x-axis of the test piece coordinate system. Equation 31 finds the unit vector $\overrightarrow{x_u}$ along x- axis.

$$\overrightarrow{x_u} = \frac{AA-TS}{\|AA-TS\|} \text{.....Equation 31}$$

AI is the 3rd reference point taken on the test piece. Equation 32 finds a support axis $\overrightarrow{y_{temp}}$ which defines the plane orientation.

$$\overrightarrow{y_{temp}} = \frac{AA-AI}{\|AA-AI\|} \text{.....Equation 32}$$

Equations 33 and 34 define the unit vector $\overrightarrow{z_u}$ along z-axis which is perpendicular to the x-y plane.

$$\vec{z} = \overrightarrow{y_{temp}} \times \overrightarrow{x_u} \text{.....Equation 33}$$

$$\overrightarrow{z_u} = \frac{\vec{z}}{\|\vec{z}\|} \text{.....Equation 34}$$

Equations 35 and 36 define the unit vector $\overrightarrow{y_u}$ along the y-axis which is perpendicular to the plane.

$$\vec{y} = \overrightarrow{z_u} \times \overrightarrow{x_u} \text{ ... ...Equation 35}$$

$$\overrightarrow{y_u} = \frac{\vec{y}}{\|\vec{y}\|} \text{.....Equation 36}$$

The 3×3 rotation matrix R below describes the orientation of the test piece with respect to the camera coordinate system. The rotation matrix contains all the unit vectors obtained using the above equations. These unit vectors are also called the direction vectors. Each direction vector defines the angle of that axis with the three axes of the camera coordinate system.

$$R = [\overrightarrow{x_u} \quad \overrightarrow{y_u} \quad \overrightarrow{z_u}] \text{.....Equation 37}$$

Equation 38 transfers the point x_c to the test piece coordinate system. Where x_c is the point with respect to the camera coordinate system is and x_l is the point with respect to the test piece coordinate system.

$$x_l = R \times (x_c - AA) \text{.....Equation 38}$$

10. Assessing the accuracy of the stereoscopic camera and IMU system

Experiment 1: The accuracy of the stereoscopic positioning system was tested by mounting two infrared LEDs on a bar at a fixed separation distance of 245 mm. The bar was moved manually through 2000 locations within a conical area subtending an angle of maximum ±70º up to a maximum distance of 5m. The distance between the two LEDS was computed by the tracking system. The RMS distance error found was 0.978mm and the variance was 0.9188mm. The error is within ±2mm of the actual distance between the LEDs, see Figure 11. The trials were repeated 15 times with the same results.

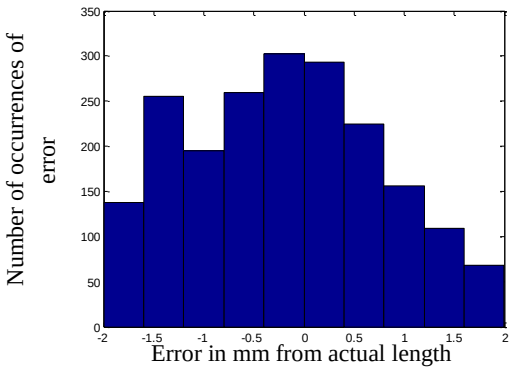

Figure 11. Error in measuring distance between two LEDs when moved around in the visible workspace (2000 locations)

Experiment 2: The two LEDs on a bar were kept stationary on a straight line at distances starting from 500 mm to 2500 mm from the Stereo vision system. At a distance of 0.5m the system accurately measured the distance between the two LEDs with zero error. At 1.5m distance the variance was 0.0085mm. At 2m distance the variance was 0.0092mm.

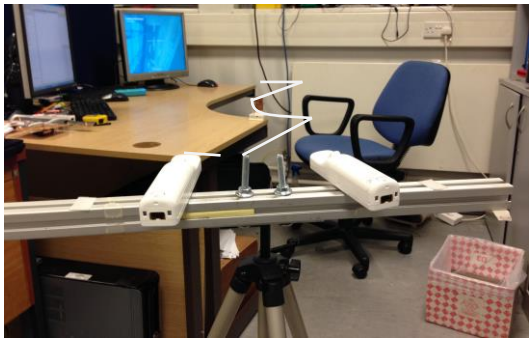

Figure 12.Stereoscopic optical system uses two Wii infra-red cameras and a single LED as target

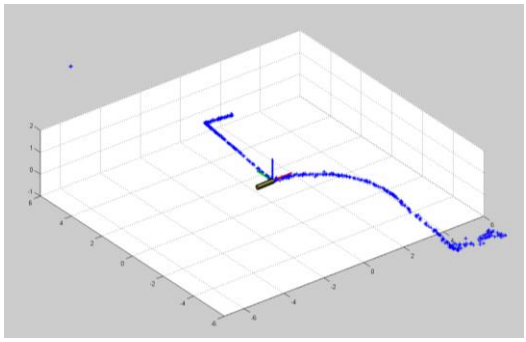

Figure 13. 3D Trajectory scan of the edge of the desk

Experiment 3: A single LED marker was moved along the edge of a table (trajectory marked by white line in Figure 12). The infrared camera was calibrated and the table coordinate system was defined by taking 3 points on the table edges. The real-time tracking of the edge is shown on a 3D image in MATLAB (Figure 13).

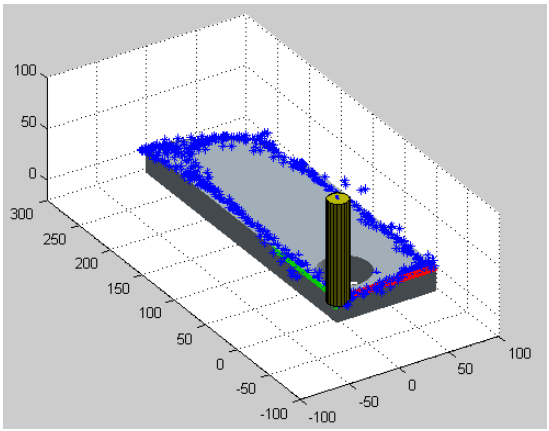

Figure 14. Real-time trajectory tracking

Experiment 4: Testing the ability of the system to record a real-time trajectory of a NDT probe on the CAD of a test object. The 3D CAD data of the test piece (shown in Figure 2) was imported into a MATLAB environment (Figure 3) as an ASCII STL (or Pro/E render SLP) file. The UT probe was moved manually on the surface of the test object. Data points on the recorded trajectory in Figure 14 are marked with asterisks. Figure also 14 shows the coordinates when the probe was lifted off the surface.

Table 1 shows the (x, y, z) data of two points at a distance of 300mm located by the stereoscopic tracking system on the test piece. The computed length between the points is 301.5291 with error of -1.5292mm.

Table 1. Measurement of two points 300mm apart

	Point 1mm	Point 2 mm	Computed length	Error (mm)
x	912	62.4888	301.5292 mm	-1.5292
y	-214.1	-191.5649		
z	1064.5	765.1761		

A distance of 670mm between two points on a desk was computed by the stereoscopic system as shown in Table 2. The computed length was 669.0620mm with error -0.938mm. This experiment was repeated 20 times with similar results.

Table 2. Location of two points on a desk at a separation distance of 670mm

	Point 1 (mm)	Point 3(mm)	Computed length	Error (mm)
x	-177.9	489.6	669.0620 mm	-0.938
y	-296.3	-251.4		
z	2409.4	2406.7		

Table 3 shows the numeric value of the rotation measured by the IMU when the probe is rotated by 0^0, 90^0 and -90^0 around the X, Y and Z axis respectively.

Table 3. Measurement of probe rotation angles with the IMU

Axis	Rotation 0^0	Error at 0^0	Rotation 90^0	Error at 90^0	Rotation -90^0	Error at -90^0
x	-0.0455	0.0455	90.6222	0.6222	-90.5527	0.5527
y	0.0492	-0.0492	89.4497	0.5503	-89.3466	-0.6534
z	-0.0386	0.0386	90.0951	-0.0951	-90.6934	0.6934

11. Combination of stereo Wii cameras, the IMU and UT system

Experiment 5: The complete system was tested on a known test piece 2. An Olympus V-126, 5 MHz ultrasound contact probe with element size 0.375 was used throughout the experiment. The probe was calibrated with test piece 2 (aluminium bar) shown in Figure 15. Test piece 2 has 7 side holes and 4 bottom holes drilled in known positions. The full specification of test piece 2 is given in table 4.

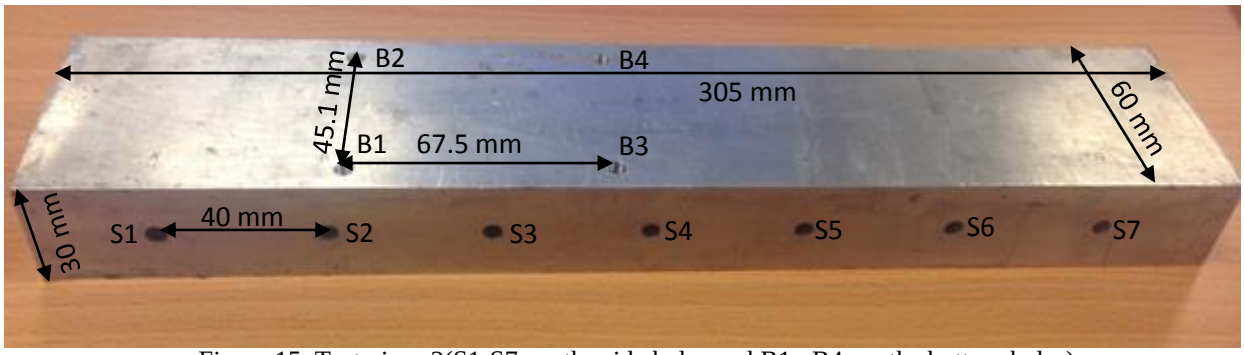

Figure 15. Test piece 2(S1-S7 are the side holes and B1 –B4 are the bottom holes)

Table 4. Dimension of the Test Piece 2

Dimension	**Bottom hole 1 position**	**Bottom hole 2 position**	**Bottom hole 3 position**	**Bottom hole 4 position**
Width: 60 mm	X=6.8 mm	X=51.9 mm	X=6.8 mm	X=51.9 mm
Length: 305 mm	Y=73 mm	Y=73 mm	Y=140.5 mm	Y=140.5 mm
Height: 30 mm	Diameter : 3.77 mm height: 9 mm	Diameter : 3.77 mm height: 9 mm	Diameter : 3.77 mm height: 9 mm	Diameter : 3.77 mm height: 9 mm
Side hole 1 position	**Side hole 2 position**	**Side hole 3 position**	**Side hole 4 position**	**Side hole 5 position**
Z=12.5 mm	Z=12.5 mm	Z=12.5 mm	Z=12.5 mm	Z=12.5 mm
Y=29.65 mm	Y=69.65 mm	Y=109.65 mm	Y=149.65 mm	Y=189.65 mm
Diameter : 4.69 mm height: 19 mm	Diameter : 4.69 mm height: 19 mm	Diameter : 4.69 mm height: 19 mm	Diameter : 4.69 mm height: 19 mm	Diameter : 4.69 mm height: 19 mm
Side hole 6 position	**Side hole 7 position**			
Z=12.5 mm	Z=12.5 mm			
Y=229.65 mm	Y=269.65 mm			
Diameter : 4.69 mm height: 19 mm	Diameter : 4.69 mm height: 19 mm			

A raster scan was performed on test piece 2 to find the side holes and bottom holes, Figure 16 shows the graphics for the complete system where the LEDs viewed by the left (image A) and right cameras (image B), the UT pulse echoes (image C) , the CAD of a test object shows the UT probe position and orientation relative to the object (image D), c-scan contour graph of the detected side holes and the bottom holes, c-scan of the detected Side hole and bottom hole (image F) and 3D visualization of the side holes and the bottom holes of position from the surface (image G).

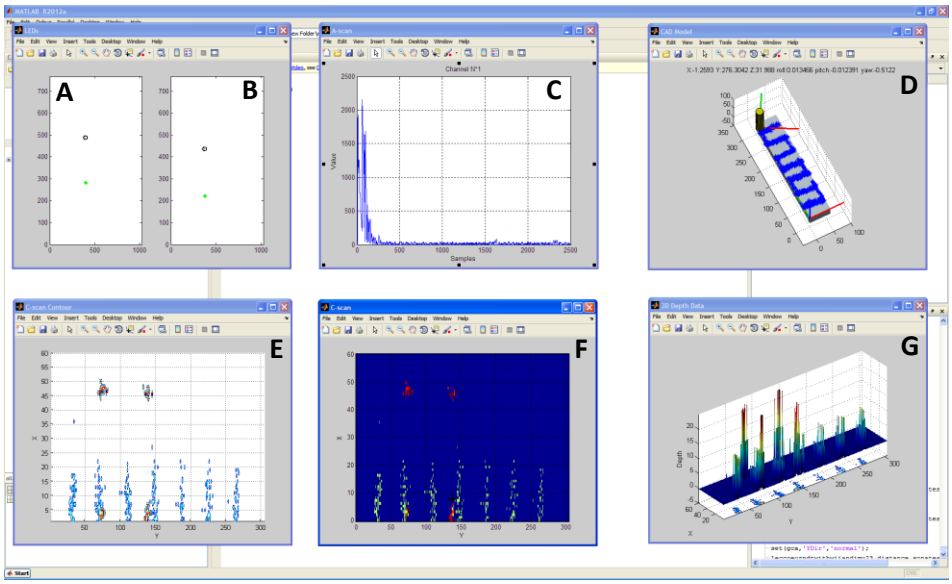

Figure 16. Graphic for the complete tracking and NDT system inspection on test piece 2

All seven side holes and four bottom holes have been identified by the system (Figure 17). Figure 18 shows 3D visualization of the side holes and the bottom holes from the surface of test piece 2. Figure 19 shows the volumetric visualization of the side holes (indicated by blue colour) and the bottom holes (indicated by brown colour) of tests piece 2 in 3D where depth data was colour coded.

Figure 17. C-scan of the detected Side holes (indicated by red circle) and bottom holes (indicated by green rectangle)

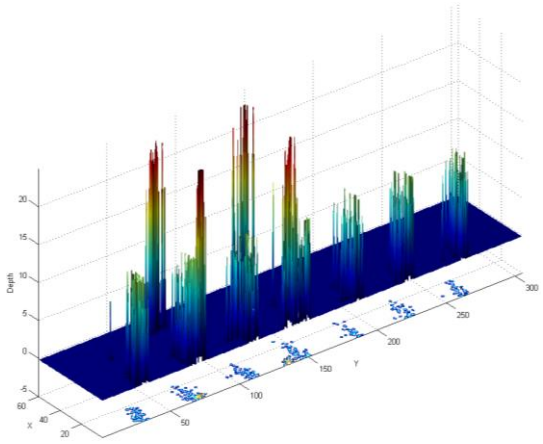

Figure 18. 3D visualization of the side holes and the bottom holes from the surface of test piece 2

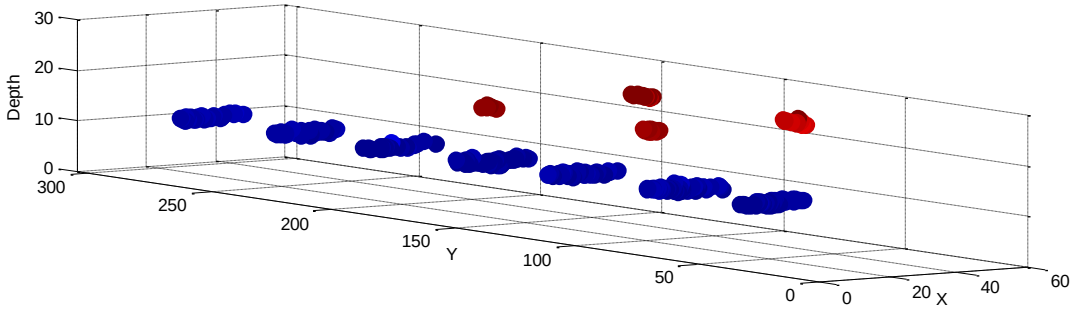

Figure 19. Scatter plots of the final 3D data volumes obtained from the postioning and c-scan data on test piece 2

The location and the depth of the side holes and the bottom holes are measured by the system shown in table 5. Measurement error while finding the location and the depth of the side holes and bottom holes are also shown in table 5.

Table 5. Experiment result on the test piece 2

	Depth (mm)	X (mm)	Y (mm)	Error(depth) (mm)	Error (X) (mm)	Error(Y) (mm)
Bottom hole 1	22.83	5.1	74.24	1.83	-1.715	1.24
Bottom hole 2	21.49	50.1	72.24	0.49	-1.8	-0.76
Bottom hole 3	20.86	6.1	139.5	-.014	-0.7	-1
Bottom hole 4	22.08	47.8	139.5	1.08	-4.1	-1
	Depth	**Length along x axis (mm)**	**Y (mm)**	**Error(depth) (mm)**		**Error(Y) (mm)**
Side hole 1	12.798	approximately 19	30.1	0.298		0.45
Side hole 2	12.976	approximately 19	69.23	0.476		-0.42
Side hole 3	12.719	approximately 19	110.4	0.219		0.75
Side hole 4	12.818	approximately 19	149.5	0.318		-0.15
Side hole 5	12.857	approximately 19	189.6	0.357		0.15
Side hole 6	12.917	approximately 19	229.8	0.417		-1.95
Side hole 7	12.956	approximately 19	267.9	0.456		-1.75

Experiment 6:

The complete system was tested on a known test piece 3. An Olympus V-126, 5 MHz ultrasound contact probe with element size 0.375 was used throughout the experiment. Ultrasound probe has been calibrated with a known test block before the experiment. In this experiment a test piece 3 (aluminium bar) has been used [Figure 20]. Test piece 3 has 2 bottom hole drilled into known position. The full specification of the test piece 3 is given in table 6.

Table 6. Specification of the Test Piece 3

Dimension	**Bottom hole 1 position**	**Bottom hole 2 position**
Width: 75 mm	X=36 mm	X=34 mm
Length: 153 mm	Y=45 mm	Y=94 mm
Height: 38 mm	Diameter : 7.43 mm height: 12.18 mm	Diameter : 7.43 mm height: 11.30 mm

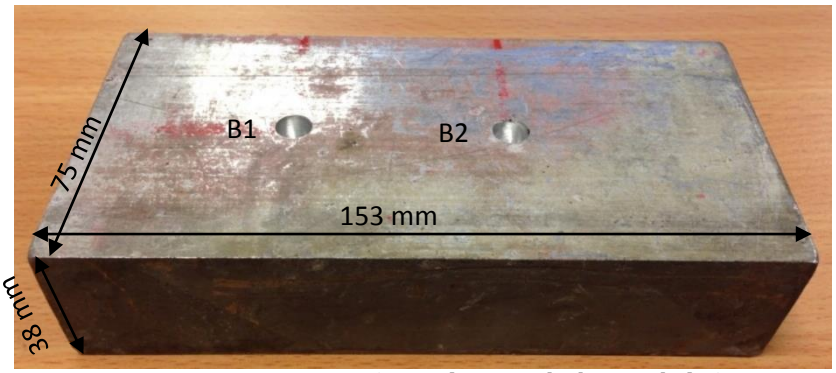

Figure 20. Test piece 3 (B1 and B2 are the bottom holes)

Figure 21 shows the graphics for the complete system where the LEDs viewed by the left (image A) and right cameras (image B), the UT pulse echoes (image C) , the CAD of a test object shows the UT probe position and orientation relative to the object (image D), c-scan contour graph of the detected side holes and the bottom holes, c-scan of the detected bottom hole (image F) and 3D visualization of the bottom holes of position from the surface (image G).

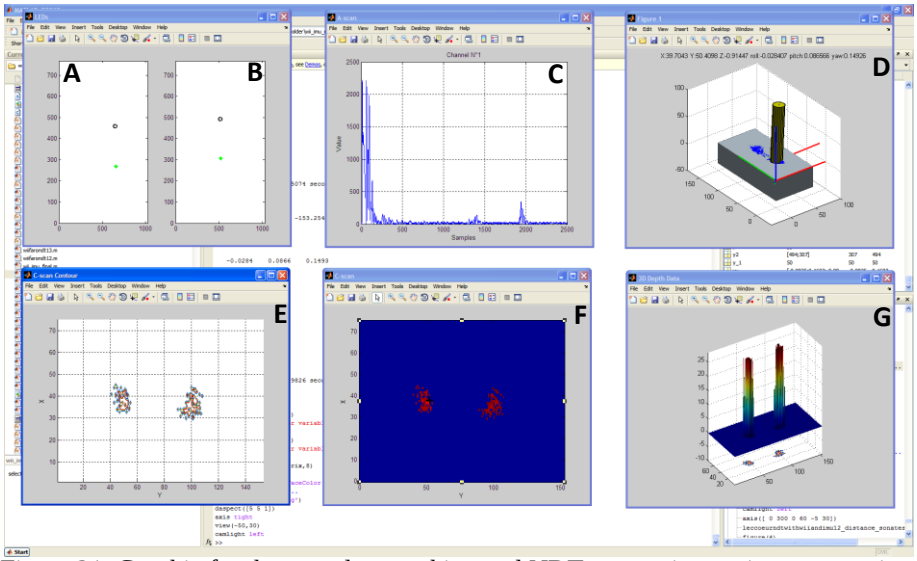

Figure 21. Graphic for the complete tracking and NDT system inspection on test piece 3

The location and the depth of the bottom holes are measured by the system shown in table 7. Measurement error while finding the location and the depth of the bottom holes are also shown in the table 7.

Table 7. Experiment result on the test piece 3

	Depth (mm)	X (mm)	Y (mm)	Error(depth) (mm)	Error (X) (mm)	Error(Y) (mm)
Bottom hole 1	27.18	37.5	46.3	1.36	1.54	1.3
Bottom hole 2	27.9	33.45	93.61	-0.2	1.2	-0.39

Figure 22 shows the c-scan of the detected bottom holes on the test piece 3. Figure 23 shows the 3D visualization of the bottom holes position from the surface of test piece 3. Figure 24 shows the volumetric visualization of the bottom holes (indicated by green and red colour) of tests piece 3 in 3D where depth data was colour coded.

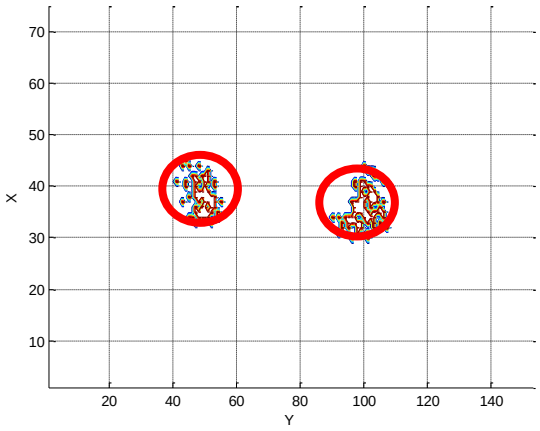

Figure 22. C-scan of test piece 3 (indicated by red circle)

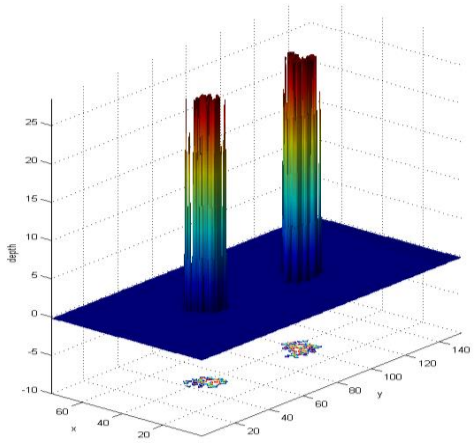

Figure 23. 3D visualization of the bottom holes of position from the surface of test piece 3

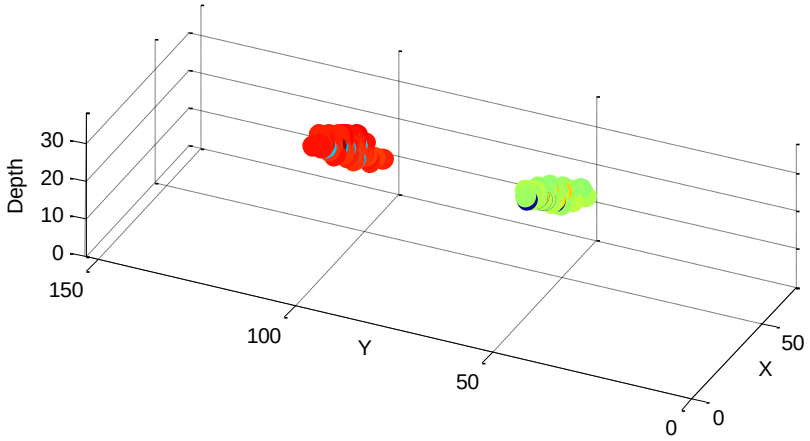

Figure 24. Scatter plots of the final 3D data volumes obtained from the postioning and c-scan data on test piece 3

12. Conclusion

An inexpensive and wireless tracking system has been developed that finds the 3D orientation and position of a NDT probe to within ±2mm over a maximum range of 5m. The system will find application both in mapping a complex surface that is to be inspected with ultrasound testing and checking that the scanning trajectories required by a qualified inspection procedure have been correctly followed. Future work will apply it to automate ultrasonic NDT and develop a training environment for novice operators. The system developed here could be used to determine the cause of loss of UT signal. Since the position and orientation of the UT probe relative to a test object is known in real time, it should be possible to know when the probe has lifted off the test surface, when the probe is no longer normal to the surface, and when the probe/surface contact force (in a spring mounted setup) has decreased below a threshold by computing distance between the LEDs and the test surface. The A-scan signal can be related to these situations to build an intelligent probe monitoring system.

13. References

1 B. McGrath, G. Worrall, and C. Udell, Programme for the Assessment of NDT in Industry 3 (PANI 3), HM Government, *Health and Safety Executive* (2005).

2 B.S. Dhillion and Y. Liu, Human error in maintenance: *a review Journal of Quality in Maintenance* 12: 21-36 (2006).

3 A.W. Elbern, and L. Guimaraes, Synthetic aperture focusing technique for image restauration. *NDT. net*, (2000). Vol.5 No.08.

4 G. Passi, M. Kritsky and Y. Shoef, High-reliability manual ultrasonic inspection. *Insight: Non-Destructive Testing and Condition Monitoring*, Vol. 41 (1999).

5 NDT Consultants. *Free Scan*. [Online] (http://www.ndt-consultants.co.uk/NDTweb/products/freescan.htm)[accessed 5 August 2014].

6 S.A. Lund, P.R. Jensen, Method and apparatus for ultrasonic examination.- *Pat.3939697 (USA)*, (1976).

7 D.Sirota, Recorder SD-22. *Operating manual*.- *Kishinev, VNIINK*, (1981).

8 F.H. Chang, J.R. Bell, A.H. Gardener, C.P. Fisher, and R.W. Haile, A laboratory mock-up ultrasonic system for composites.- *Materials Evaluation*, (1982), Vol.40, N 7, p.756-761.

9 G. Passi, M. Kritsky, and Y. Shoef, High-reliability manual ultrasonic inspection. *Insight*, (1999). 41(4): p. 225-31.

10 T. Pintaric, and H. Kaufmann. Affordable infrared-optical pose-tracking for virtual and augmented reality. *in Proceedings of Trends and Issues in Tracking for Virtual Environments Workshop, IEEE VR.* (2007).

11 "ART Advanced Realtime Tracking." *ART Advanced Realtime Tracking*. [Online] (http://www.ar-tracking.com) [accessed 5 August 2014].

12 W. Deng, B. Matuszewski, L. Shark, J. Smith and G. Cavaccini, Multi-modality NDT image fusion and its mapping on curved 3D CAD surface. In, 2004. Citeseer, (2004).

13 I. Cornwell and A. Mcnab, Towards automated interpretation of ultrasonic NDT data, NDT & E International, 32, 101-107 (1999).

14 A New Dimension in Point Cloud. *3D Measurement Technology from FARO*. [Online] (http://www.faro.com/FaroArm) [accessed 5 August 2014].

15 PhaseSpace Motion Capture. *PhaseSpace Motion Capture*. [Online] (http://www.phasespace.com/) [accessed 5 August 2014].

16 Precise Motion Capture in Any Volume Anywhere. *Vicon* [Online] (http://www.vicon.com) [accessed 5 August 2014].

17 OptiTrack Motion Capture, *NaturalPoint, Inc.* [Online] (https://www.naturalpoint.com) [accessed 5 August 2014].

18 G. Caruso and G.M. Re, AR-Mote: A wireless device for Augmented Reality environment. *In, 2010. IEEE*, 99-102 (2010).

19 S. Hay, J. Newman, and R. Harle, Optical tracking using commodity hardware. *In, 2008. IEEE*, 159-160 (2008).

20 D. Wang, and D. Huang, Low-cost motion capturing using nintendo wii remote controllers. *Csc2228 project report*, University of Toronto, Toronto, Ontario M5S 3G4 (2008).

21 S. De Amici, A. Sanna, F. Lamberti and B. Pralio, A Wii remote-based infrared-optical tracking system. *Entertainment Computing*, 1, 119-124 (2010).

22 W. Zhu, A.M. Vader, A. Chadda, M.C. Leu, X.F. Liu and J.B. Vance, Wii remote–based low-cost motion capture for automated assembly simulation. *Virtual Reality*, 1-12 (2011).

23 R. Hartley, and A. Zisserman, Multiple view geometry in computer vision. *Robotica*, (2005).

24 R. Mahony, T. Hamel, and J.-M. Pflimlin, Nonlinear complementary filters on the special orthogonal group, *Automatic Control, IEEE Transactions on*, vol. 53, pp. 1203 –1218, (2008).

25 J.L. Marins, et al. An extended Kalman filter for quaternion-based orientation estimation using MARG sensors. in Intelligent Robots and Systems, *Proceedings. 2001 IEEE/RSJ International Conference on. 2001: IEEE* (2001).

26 S.O. Madgwick , A.J. Harrison, and R. Vaidyanathan. Estimation of IMU and MARG orientation using a gradient descent algorithm. *in Rehabilitation Robotics (ICORR), 2011 IEEE International Conference on. 2011: IEEE* (2011).

27 J.Y. Bouguet, Camera calibration toolbox for Matlab, (2004).

28 T. Svoboda, D. Martinec, and T. Pajdla, A convenient multicamera self-calibration for virtual environments. Presence: Teleoperators & Virtual Environments, 14, 407-422, (2005).